Arab J. Nucl. Sci. Appl., Vol. 56, 3, 27-40 (2023)

ISSN 1110-0451

Arab Journal of Nuclear Sciences and Applications

Web site: ajnsa.journals.ekb.eg

(E S N S A)

Radiation Attenuation Properties of $BaMnO_3$ Doping Nickel Semiconductor Perovskite Using Phys-X/PSD Software

M.H. Ghozza

Basic Science Department, Marg High institute of Engineering and Modern Technology, Cairo, Egypt

ARTICLE INFO

Article history:

Received: 4th Aug. 2022

Accepted: 17th Nov. 2022

Keywords:

$BaMn_{1-x}Ni_xO_3$;

Build up factor;

Fast neutron removal cross-section;

Gamma-ray attenuation;

Perovskite;

Phy-X/PSD.

ABSTRACT

This research is focused on the effect of the nickel doping ratio on γ-ray attenuation radiological parameters for five compounds of chemical compositions $BaMn_{1-x}Ni_xO_3$ (x=0.1,0.3,0.5,0, and 0.9), named Ni1, Ni3, Ni5, Ni7, and Ni9, in energy range between 0.015 and 15 MeV utilizing Phy-X/PSD software. Radiation parameters (MAC, LAC, HVL, TVL, MFP, ACS, ECS, Z_{eff}, N_{eff}, C_{eff}, Z_{eq}, EBF, and EABF) are evaluated. Most of parameters depend profoundly on the photon energy. For instance, MAC is reduced from 137 to 0.133 cm^2/g and LAC is increased from 775.7 to 0.75 cm^{-1} with increasing E_{ph} (0.015 -15 MeV). Additionally, HVL and TVL increase from 0.0009 to 0.9 and from 0.003 to 3 cm respectively in between that energy range. Also, MFP increases from 0.001 to 1.3 cm but N_{eff}, C_{eff}, Z_{eff} , ACS, and ECS, decrease from 4×10^{24}-2×10^{24}, 1.6×10^{10}-0.7×10^{10}, 32 - 15 electron/g, 100×10^{-24}-1×10^{-24}, and 3.3×10^{-23} - 0.007×10^{-23} cm^2/g at the energy 0.015-15 MeV. Furthermore, Z_{eq} value is 19.3. Additionally, the exposure and energy absorption buildup factors (EBF and EABF) are determined to be 1-1.2, 2.7-29, 1.3-1.7, and 3.15-22 at various penetration depths (1- 40 mfp). These values are independence of E_{ph} at low mfp but at 40 mfp they are changed from 3to29. Maximum buildup parameters site in middle energy range, 0.2-1MeV. In another side, Most of such parameters are dependent on the Ni dopants. FNRCS values are 0.85 cm^{-1}. The present samples exhibit greater radiological properties than that published previously. These investigations are critical for the development of utilized semiconductor as detectors, attenuators, and protection radiation in various radiation safety applications fields.

1. INTRODUCTION

Ionizing radiation is harmful and may be encountered in a variety of situations, including nuclear power plants, accelerators, industrial dosimetry, research labs, agriculture, space technology, radiotherapy, and nuclear medicine. All types of ionizing radiation, involving radioactive decay in radiation sources, characteristic X-rays, neutron inelastic scattering, virtually always emit gamma radiation and X-rays [1-3]. When such radiation interacts with live or nonliving materials, it can cause heating, chemical bond breakdown, or ionization of molecules, resulting in the release of ionized species. The energy of the incident radiation and the substance exposed mostly determine how much damaging ionizing radiation is present. Gamma radiation is the most penetrating of the ionizing radiation types [4]. It is critical to take preventive steps to protect workers and the public against high-energy radiation exposure [1]. Gamma ionizing radiation is the most penetrating of the ionizing radiation type. A dense medium, such as a thick concrete shield or any lead-based material, can inhibit gamma [4]. Shielding properties of new materials have become increasingly significant in determining the best appropriate material for environmental protection [2]. lead and cement-based materials are particularly recommended for this [1]. Furthermore, a study of photon interactions with matter becomes critical since it is required in various applications such as medical dosimetry, radiation shielding, and industrial [5]. Lead and Concrete are popular shielding material because of their exotic properties such as its poisonousness and Lead's low melting point of 327.5°C. But concrete has high mechanical strength, low cost, and ease of upkeep

Corresponding author: mghozza2@gmail.com

DOI: 10.21608/ajnsa.2022.154447.1621

and is a blend of light and heavy nuclei that has outstanding neutron and gamma ray attenuation qualities from the shielding standpoint [6-9].

Several studies focused on developing novel materials with optimum and perfect qualities for use as radiation shields [5]. To understand radiation dosimetry, it is essential to understand how energy is transmitted and absorbed when photons interact with materials. One of the crucial elements in radio physics and chemistry is the attenuation coefficients of semiconductor materials used to calculate energy deposition and photon penetration in shielding and dosimetry materials. As a result, knowing its exact value will assist in a variety of professions [5]. Many materials have been developed for shielding different radiations, including concrete [10,11], polymer composites [7], glass [12], serpentine ($Mg_3Si_2O_5$ $(OH)_4$) [13], hematite (Fe_2O_3), and barite ($BaSO_4$) minerals [14]. In addition, a new form of concrete with improved radiation shielding properties was developed. Few authors investigated the attenuation properties of semiconductor materials such as CdTe and CdZnTe [15], Cu_2MnGeS_4, $Cu_2MnGeSe_4$, and $Cu_2MnGeTe_4$ [5] for application as nuclear medicine detectors. The goal of studying attenuation qualities is to find new and acceptable semiconductor materials for applications in various nuclear aspects.

One of two things can happen when a photon with energy E passes through a material with atomic number Z: either it passes through unaffected, or it interacts with the material in a variety of ways, such as photoelectric absorption, Compton scattering, and the pair-production effect, which results in absorption or attenuation [16].

The energy range may be separated into three regions based on how gamma radiation reacts with various materials. The photoelectric effect, where photons are absorbed by transferring all of their energy to a single electron in the outer atomic shells, is the predominant process in the low-energy zone. In the intermediate energy, photon scattering is mostly caused by the Compton scattering mechanism, while a photon is scattered by a nearby free atomic electron producing an attenuated photon and a scattered electron [2]. Numerous authors are interested in determining the effective atomic numbers (Z_{eff}) for interactions between photons, electrons, protons, alpha particles, and carbon ions on a variety of materials, including glasses and dosimetry materials [17]. The study of "buildup factors," sometimes known as "radiation dosage," gives a significant information on how radiation interacts with optical materials [18]. A useful method for evaluating a substance's capacity to attenuate neutrons is the fast neutron removal cross-section (FNRCS) [19].

In the present work, the radiation attenuation properties have been performed for five nickel doping composites $BaMn_{1-x}Ni_xO_3$ (x=0.1,0.3,0.5,0.7, and 0.9) named Ni1, Ni3, Ni5, Ni7, and Ni9 as nano semiconductor materials prepared using coprecipitation method [20]. The Phy-X/PSD program [19, 21] could be used to calculate all photon-shielding parameters. Mass attenuation coefficient, MAC, linear attenuation coefficient LAC, half value layer HVL, the 10^{th} value layer TVL, mean free path MFP, total atomic cross section ACS, electronic cross section ECS, effective atomic number Z_{eff}, effective electron density N_{eff}, effective conductivity C_{eff}, equivalent atomic number Z_{eq}, exposure build factors EBF, and exposure absorption build factors, EABF besides, fast neutron removal cross section FNRCS of perovskite have been calculated in this study utilized to build radioactive devices as well as study effect of nickel doping ratio on these parameters particular in nanosized particles.

2. MATERIALS AND METHOD

Phy-X/PSD computer programs were used in this study to examine the γ- radiation interaction and shielding parameters of the five distinct perovskite nanocomposites. Most γ- radiation interaction and shielding characteristics have been successfully measured by these user-friendly computer programs over a variety of energy ranges (0.015 to 15 MeV) [19].

3. RESULTS AND DISCUSSION

3.1. Radiation shielding parameters based on nuclear characteristics

The photoelectric effect, Compton scattering, and pair production of the photon-matter interaction phenomena predominate in three different energy regions, according to research on the gamma attenuation properties of the materials in the photon energy range of 0.015 - 15 MeV. If an incoming photon (I_o) travels through an attenuator with a thickness of x (cm) and transmitted photon intensities of x (cm) (I). LAC, which is based on photon energy and material constituent elements, it can be determined using the formula below (Lambert-Beer law) [22].

$$I = I_o e^{-\mu x}, \qquad (1)$$

Additionally, MAC values offer crucial details about the radiation-shielding materials. The following equation

explains the candidate samples for compound and mixture materials, which may be found simply by dividing over, (MAC= μ /ρ), where w_i indicates the proportion of the weight of the i^{th} element in composite.

$$MAC = \left(\frac{\mu}{\rho}\right) = \sum_i w_i(\mu/\rho)_i, \qquad (2)$$

Based on the candidate program, the values of LAC versus $E_{ph,}$ ranging from 0.015 to 15 MeV is presented in Fig. 1. LAC values decrease more quickly with increasing E_{ph}. Also, as shown in Fig. 1 and Table 1, the LAC value primarily depends weakly on the nickel doping ratio (x) which is ascribed to increase of sample density range (ρ_{Ni1} = 5.451- ρ_{Ni9} = 5.630 g/cm^3). Therefore, one can deduce that the high-density samples can absorb gamma rays efficiently providing such materials with a variation of industrial and health requests [23].

The fluctuation of MAC with E_{ph} is shown in Fig. 2. At E_{Ph} = 0.1 MeV, MAC Ni9 sample, high density, has the greatest MAC values, whilst the Ni1 has the lowest. The photoelectric effect dominates in that energy region, and the cross-section of absorption (σ_a) is proportional to $E^{-3.5}_{ph}$ [24] and the atomic numbers (Z^4 or Z^5) of the atoms in a sample [25,26]. Because the Compton scattering process dominates (σ_{com}~E^{-1}) in the intermediate energies (0.4-5 MeV), MAC displays a slighter drop with increasing incoming energy, where the cross-section decreases exponentially with energy and is proportional to Z [27]. The dominance of absorption over scattering and resulting rather constant behavior at high energy (above 5 MeV) (σ_{pp}~logE) are caused by pair production. Furthermore, the results showed that the MAC is directly proportional to excess nickel ratio in the. Similar results have been obtained when studying shielding radiation characteristics of different alloys [25]. As demonstrated in Table 1, the current work's MAC and LAC magnitude are greater than those of normal concrete, steel-magnetite, and heavy concrete kinds widely used for protective reasons [16, 28]. MFP is readily determined by inverting the total linear attenuation coefficient from Eq. 3, it is the average distance between two successive photon interactions with material that causes a drop in the intensity of the input photon beam by a factor of 1/E [29,30];

$$MEP = \frac{1}{\mu}, \qquad (3)$$

MFP depends weakly on both photon energy and nickel doping ratio. From Fig. 3, no significant change in MFP with different (x), at different E_{ph} i.e, 0.1, 1, 10 MeV, MFP decreases about 7% with increasing nickel dopant from 0.1 to 0.9. As a result, at the higher sample density, the attenuation performance improved. Table 1 compares MFP values of our samples at 0.1, 10, and 15 MeV to those of previous studies, regular concrete, and steel-magnetite (heavy concrete) [28]. HVL and TVL, are defined as the sample thickness required to reduce photon intensity by 1/2 and 1/10 of its original value respectively, they can be calculated using eq. (4), (5) [5].

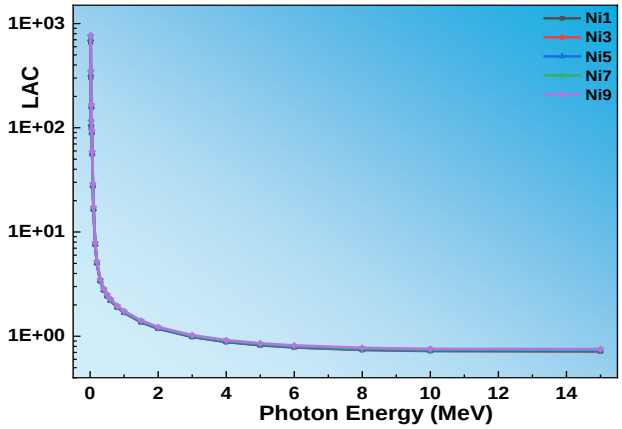

Fig. (1): Photon energy vs. LAC of samples

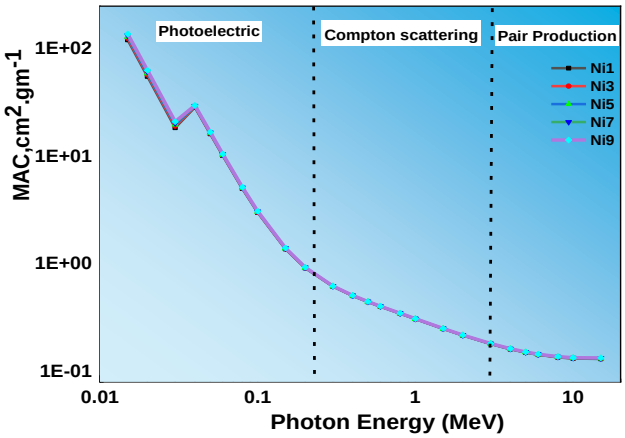

Fig. (2) Photon energy vs. MAC of samples

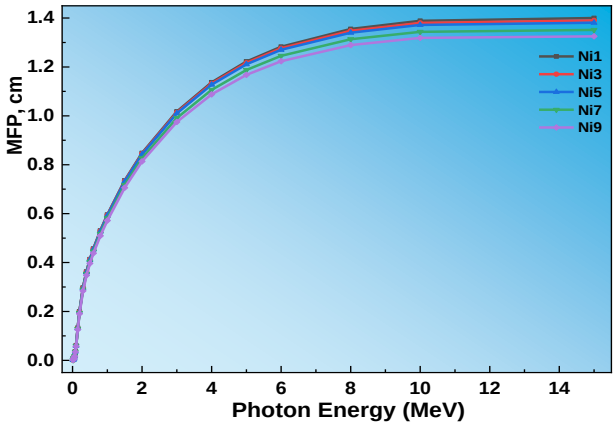

Fig. (3): Photon energy vs. MFP of samples

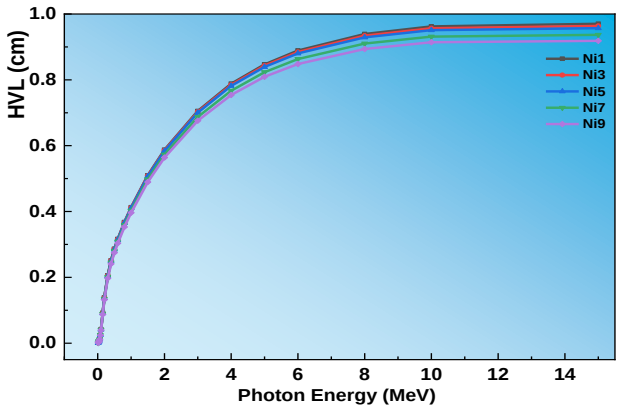

Fig. (4) photon energy vs. HVL of samples

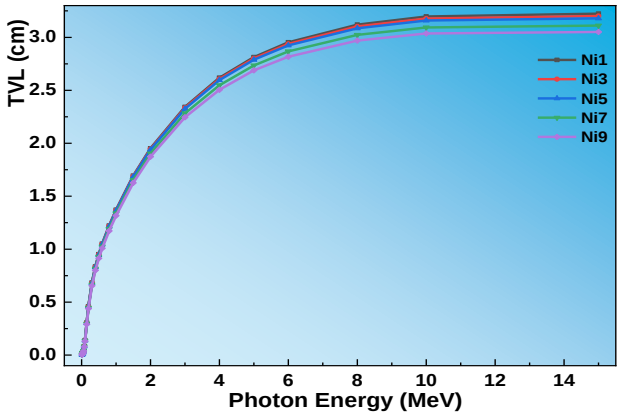

Fig. (5): photon energy vs. TVL of samples

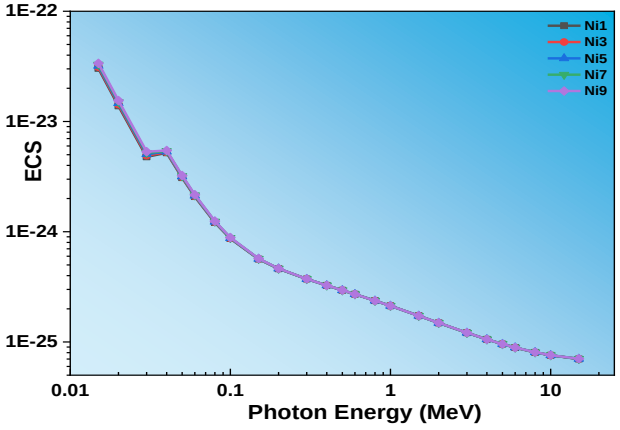

Fig. (6): photon energy vs. ECS of samples

$$HVL = \frac{ln2}{\mu}, \qquad (4)$$

$$TVL = \frac{ln10}{\mu}, \qquad (5)$$

For all semiconductor samples, the HVL values are dependent on E_{ph}, as shown in Fig. (4). When E_{ph} is increased to 3 MeV, its values significantly increase. Following that, as the E_{ph} is increased up to 10 MeV, the HVL slowly grows. Beyond this energy,10 MeV, HVL behaves in a consistent manner. Its values were obtained at 0.015 and 15 MeV, corresponding to 0.001, 0.001, 0.0009, 0.0009, and 0.0008 cm for Ni1, Ni3, Ni5, Ni7, and Ni9 samples, respectively, and 0.97, 0.963, 0.957, 0.936, and 0.918 cm for Ni1, Ni3, Ni5, Ni7, and Ni9 semiconductor samples. These values are quite similar to those obtained by N. Sabry et al. for Cu_2MnGeS_4 (0.003 cm), $Cu_2MnGeSe_4$ (0.002 cm), and $Cu_2MnGeTe_4$ (0.002 cm) [9]. At a maximum photon energy of 15 MeV, the HVL of all samples increases by nearly 1000 times. Therefore, samples with low density have the greatest HVL value, and vice versa, as high-energy photons will be absorbed by thick sample layers. Otherwise, a sample with a high density has a better chance of absorbing photons than others. TVL as a function of E_{ph} provides instant feedback on the size or thickness of the specimen, which can block up to 90% of input photons. The same tendency of HVL is shown in Fig.5, where the variance of HVL and TVL with density is very small in all energy ranges. They, on the other hand, are heavily reliant on E_{ph} [31]. The investigation of radiation shielding materials, Z_{eff} and N_{eff} are also relevant factors. To get the Z_{eff} values, first calculate the ACS (σ_a) and ECS (σ_e) values with Eq. 6 and Eq. 7[32, 33]. The probability of interaction per electron in a unit volume may be determined using the *ECS* formula.

$$ACS = \sigma_a = \sigma_m \frac{1}{\sum_i n_i} = (\mu/\rho)_{target}/N_A \sum_i \frac{w_i}{A_i}, \qquad (6)$$

$$ECS = \sigma_e = \frac{1}{N_A}\sum_i \left(\frac{\mu}{\rho}\right)\frac{f_i A_i}{z_i}, \qquad (7)$$

where σ_m means molecule cross-section, A_i denotes atomic weight, w_i denotes for each target element's fractional weight, and N_A denotes Avogadro's constant.

The number of atoms and electrons in a unit volume of a substance will increase ACS and ECS of that substance. In terms of radiation shielding, materials with high ACS and ECS are superior. Figs. (6,7) indicate that ACS and ECS behave similarly across the whole energy range. ACS and ECS depend on the chemical makeup of the material and the incident E_{ph}, which explains the similarities. This differs from the findings of Bashter et al. [16], which uses a different chemical composition, whereas the chemical composition does not alter in our work. Figs. (6,7) sho that the examination of the Ni9 sample yielded the highest ACS and ECS values, whereas the N1 sample yielded the lowest. Furthermore, as E_{Ph} rises, these values drop. For example, at 0.015, 1, and 15 MeV, Ni1 samples had ACS values of 900×10^{-24}, 2.4×10^{-24}, and 1×10^{-24} cm^2 /g, while N9 samples have

ACS values of 1070×10^{-24}, 2.4×10^{-24}, and 1×10^{-24} cm^2 /g. N1 has ECS values of 30×10^{-24}, 0.21×10^{-24}, and 0.075×10^{-24} cm^2 /g at 0.015, 1 and 5 MeV, but N9 has ECS values of 33×10^{-24}, 0.21×10^{-24}, and 0.075×10^{-24} cm^2 /g at the same energies. Z_{eff} is estimated by following Eq. 8 [34]: The other quantity, the electron density (N_{eff}), measures the electron numbers per unit mass of the interacting target and can be calculated as follows [35]:

$$Z_{eff} = \frac{\sigma_a}{\sigma_e}, \quad (8)$$

$$N_{eff} = N\frac{Z_{eff}}{\sum_i f_i A_i}, \quad (9)$$

Table (1): Comparison between Gamma attenuation coefficient of $BaMn_{1-x}Ni_xO_3$ and other published materials

Sample	Density, ρ (g/cm^3)	MAC, (g/m^3)			LAC, (cm^{-1})			MFP, (cm)			Ref.
		0.1 MeV	10 MeV	15 MeV	0.1 MeV	10 MeV	15 MeV	0.1 MeV	10 MeV	15 MeV	
Ni1	5.451	3.008	0.132	0.131	16.397	0.720	0.714	0.061	1.388	1.400	Present work
Ni3	5.458	3.029	0.133	0.131	16.536	0.725	0.719	0.060	1.380	1.390	
Ni5	5.465	3.051	0.133	0.132	16.766	0.729	0.724	0.059	1.371	1.380	
Ni7	5.554	3.072	0.134	0.133	17.065	0.744	0.740	0.058	1.343	1.351	
Ni9	5.632	3.094	0.135	0.134	17.427	0.758	0.755	0.057	1.318	1.325	
Cu_2MnGeS_4	4.11	0.373	0.029	0.030	1.535	0.120	0.122	0.652	8.368	8.172	[9]
$Cu2MnGeSe_4$	5.29	0.553	0.031	0.033	2.924	0.167	0.175	0.342	6.033	5.707	[9]
$Cu2MnGeTe_4$	5.91	1.355	0.036	0.039	8.005	0.213	0.232	0.125	4.705	4.305	[9]
Ordinary concreate	2.3	0.173	0.023	0.021	0.397	0.053	0.049	2.607	18.88	20.408	[16]
Steel-magnetic concrete	5.11	0.325	0.028	0.029	1.661	0.144	0.146	0.848	6.944	6.849	[16]

Table (2): FNRCS coefficient of present samples comparison with other materials

No.	Samples	FNRCS, cm^{-1}	Cryst. Size, nm	MFP, cm At 5 MeV	HVL, cm At 5 MeV	Ref.
1	Ni1	0.843	77.0	1.22	0.84	Present work
2	Ni3	0.842	90.2	1.21	0.84	
3	Ni5	0.841	48.4	1.21	0.83	
4	Ni7	0.854	45.7	1.18	0.82	
5	Ni9	0.864	36.8	1.16	0.80	
6	Cu_2MnGeS_4	0.089		7.94	5.42	[9]
7	$Cu_2MnGeSe_4$	0.094		6.33	4.31	
8	$Cu_2MnGeTe_4$	0.090		5.15	3.61	
9	Ferrite	0.141		6.24	4.31	
10	Chromite	0.131		6.70	4.57	
11	Magnetite	0.139		6.56	4.33	
12	Barite	0.100		6.72	4.60	
13	RS-520	0.068		4.42	2.53	
14	RS-360	0.064		6.57	4.51	
15	RS-253-G18	0.089		13.61	9.50	
16	Graphite	0.065				[42]
17	Concrete	0.100				
18	Fe	0.166				
19	Cu_2CoGeS_4	0.093				[43]
20	$Cu_2CoGeSe_4$	0.099				
21	$Cu_2CoGeTe_4$	0.092				

The close relationship between Z_{eff} and N_{eff} in Fig. (8,9) demonstrates that the values of Z_{eff} and N_{eff} depend on both energy and chemical composition. The variation of the Z_{eff} for the studied samples in the energy range 0.015–15 MeV is revealed in Fig. 8, where Z_{eff}'s value decreases as photon energy rises at lower energies; but at intermediate energies, Z_{eff} is nearly constant; and at higher energies, Z_{eff} rises slightly. For Ni1, Ni3, Ni5, Ni7, and Ni9, the Z_{eff} values at 0.015 MeV are 31.23, 31.44, 31.65, 31.85, and 32.04, respectively. This means that gamma rays have a higher chance of interacting with the Ni9 semiconductor sample and a lower chance of penetrating it. At 0.015 MeV, the Z_{eff} values for Cu_2MnGeS_4, Cu2MnGeSe4, and $Cu_2MnGeTe_4$ are 27.13, 32.11, and 39.21, respectively [5]. At 0.0148 MeV, the Z_{eff} values for CdTe and CdSe [36] are 50.4 and 39.2, respectively. $CuInSe_2$ [26] has a Z_{eff} value of 23 at 0.0142 MeV. This suggests that gamma rays have a higher chance of interacting with our samples than CuInSe2, Cu_2MnGeS_4, and $Cu_2MnGeSe_4$, but a lower chance than CdTe, $Cu_2MnGeTe_4$ semiconductor.

The N_{eff} variation for samples in the E_{ph} range of 0.015-15 MeV is revealed in Fig. 9. At 0.015 MeV, N_{eff} values for Ni1, Ni3, Ni5, Ni7, and Ni9 are 4.00×10^{24}, 4.03×10^{24}, 4.05×10^{24}, 4.07×10^{24}, and 4.09×10^{24} electron/kg, respectively, while Cu_2MnGeS_4, $Cu_2MnGeSe_4$, and $Cu_2MnGeTe_4$ have N_{eff} values of 3.41×10^{23}, 2.71×10^{23}, and 2.47×10^{23} electron/kg. N_{eff} at 0.0148 MeV is 2.5 10^{23} electron. cm^{-3} for CdSe and CdTe. N_{eff} and Z_{eff} rely on photon energy because they are inversely related to the average atomic weight of the material [37]. C_{eff} is another important factor in photon-matter interactions. This value is proportional to the number of free electrons generated per unit volume of material with associated photon energy. C_{eff} is proportional to the material density, the effective electron density N_{eff}, and the temperature of the environment in which the interaction takes place, and it is expressed by the Eq. 10 [38]:

$$\boldsymbol{C_{eff}} = \left(\frac{\boldsymbol{N_{eff}\rho e^2\tau}}{\boldsymbol{m_e}}\right)10^3, \qquad \textbf{(10)}$$

where e is an electron charge in coulombs and m_e is the mass of an electron in kilograms [39] which may be used to calculate an electron's average lifetime at the Fermi Surface:

$$\boldsymbol{\tau} = \frac{\hbar}{\boldsymbol{K_BT}} = \frac{\boldsymbol{h}}{\boldsymbol{2\pi K_BT}}, \qquad \textbf{(11)}$$

where h denotes Planck's constant in J.s, T denotes temperature in K, and k denotes Boltzman's constant in J/K.

The fluctuations in C_{eff} with E_{ph} are depicted in Fig. 10. Despite the fact that C_{eff} and N_{eff} are directly related, C_{eff} values vary with energy differently than N_{eff} due to the varied densities of the examined substances. This finding was previously researched for different alloys [6]. The production of free electrons in the zone dominated by photoelectric absorption is high as shown in Fig. 10. Photons in this range have lower energy and longer wavelengths, making them more likely to interact with electrons in the target material. Because of the increased likelihood, more photons are absorbed by electrons, resulting in more free electrons. The Ni9 semiconductor sample has the greatest C_{eff} values. C_{eff} of the examined materials are virtually independent of the E_{ph} in Compton scattering, the main energy area. The probability of interactions with the target material electrons in these locations is smaller than in the lower E_{ph} region due to the great penetration of photons. The probability of photon dispersion is indicated by the build-up factors, R and Z_{eq} parameters must be estimated to evaluate the build-up factors. R may be defined as follows by Eq. 12 [37]:

$$\boldsymbol{R} = \frac{(\boldsymbol{\mu}/\boldsymbol{\rho})_{\boldsymbol{com}}}{(\boldsymbol{\mu}/\boldsymbol{\rho})_{\boldsymbol{Total}}}, \qquad \textbf{(12)}$$

where $(\mu/\rho)_{com}$ denotes the Compton MAC and $(\mu/\rho)_{total}$ denotes the material's total MAC. R values were evaluated using the Phy-X/PSD software.

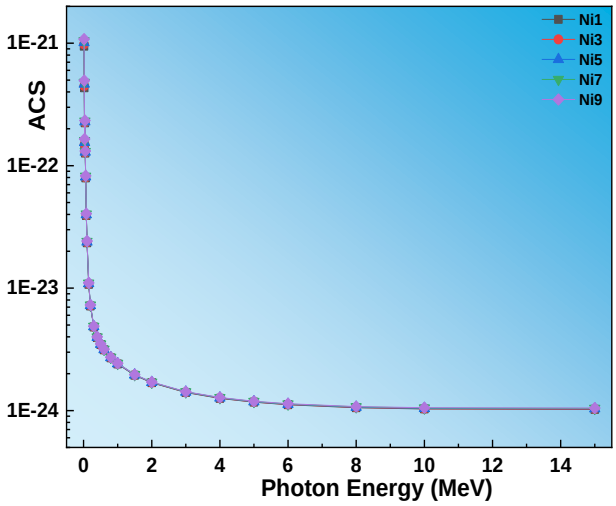

Fig. (7): photon energy vs. of ACS samples

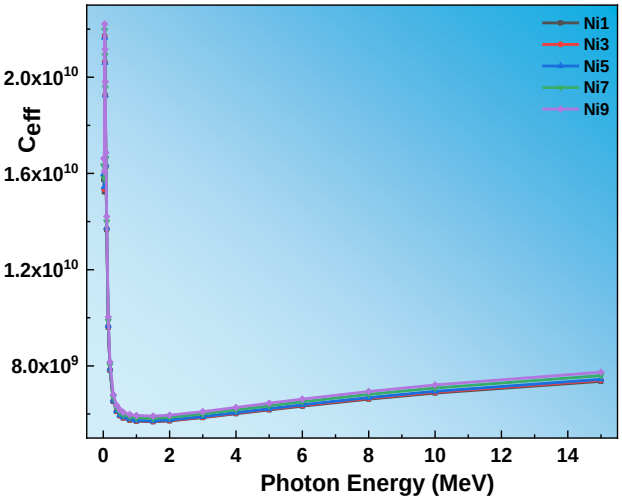

Fig. (10): photon energy vs. C_{eff} of samples

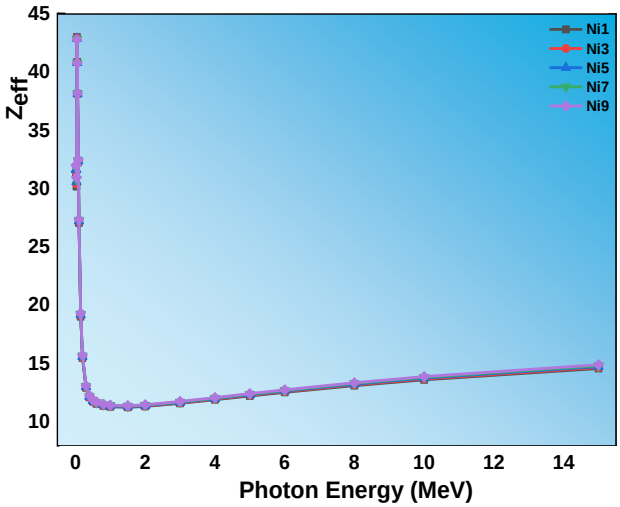

Fig. (8): photon energy vs. Z_{eff} of samples

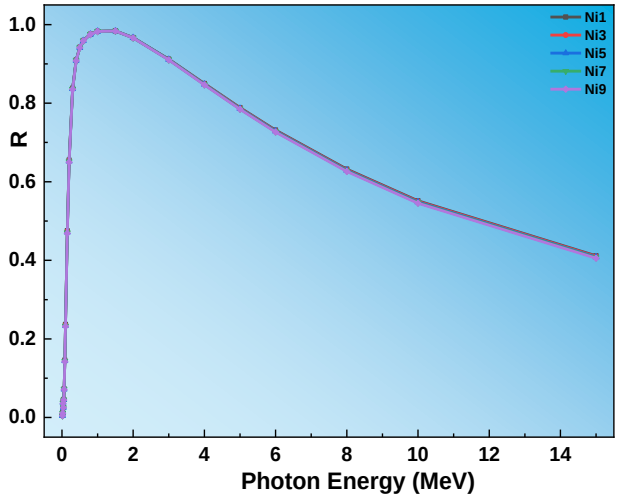

Fig. (11): photon energy vs. R ($(\mu/\rho_{com})/(\mu/\rho_{total})$) ratio of samples

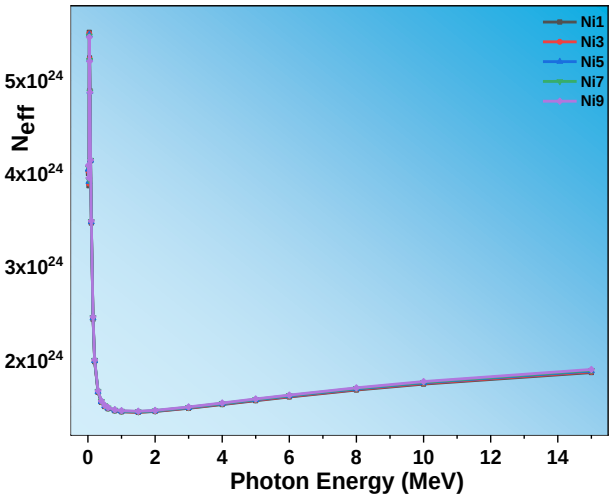

Fig. (9): photon energy vs. N_{eff} of samples

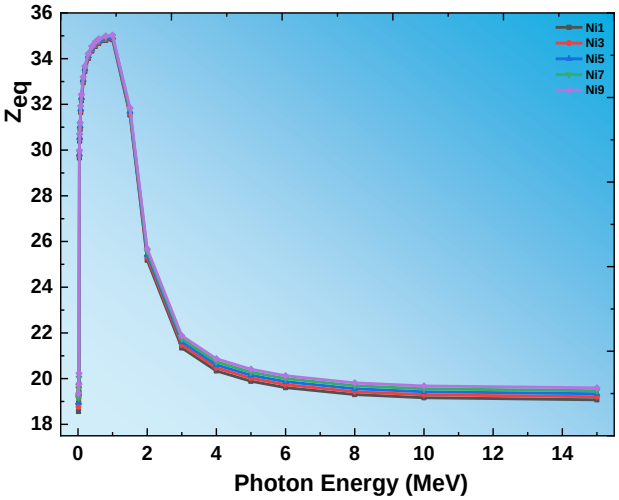

Fig. (12): Photon energy vs. Z_{eq} of samples

Fig. 11 depicts R value variance within the energy range of 0.015–15 MeV. In the intermediate energy range, Compton scattering is inelastic and dominant, but as incident energy increases, pair-production dominates and the probability of Compton scattering drops, leading to a general fall in the R values [6]. The Z_{eq} is the second parameter that must be calculated using Eq. 13[19]:

$$\boldsymbol{Z_{eq} = \frac{Z_1(logR_2 - logR) + Z_2(logR - logR_1)}{logR_2 - logR_1}}, \qquad \textbf{(13)}$$

where R_1 and R_2 values represent $(\mu/\rho)_{Com}/(\mu/\rho)$ the combined atomic weights of two Z_1 and Z_2 elements, respectively. The alterations in the Z_{eq} magnitudes of the examined samples were shown in Fig. 12. All sample Z_{eq} readings do not indicate a significant energy-dependent variability. Also, the Z_{eq} for photon energy exhibits a behavior that is quite similar to the Z_{eff} for multi-element materials, which agree with Al-Buriahi and Tonguc [40].

3.2. The energy of photons affects the EBF and EABF values.

The two categories of buildup factors are EBF and EABF. The fitting of geometric progression (G-P), which serves as a measure for the buildup factors, may be employed to ascertain the R and Z_{eq} parameters as seen in Eq. 14 [19].

$$\boldsymbol{P = \frac{P_1(logZ_2 - logZ_{eq}) + P_1(logZ_{eq} - logZ_1)}{logZ_2 - logZ_1}}, \qquad \textbf{(14)}$$

P_1 and P_2, the G–P fitting parameters, correspond to the Z_1 and Z_2 atomic numbers, respectively. EABF and EBF values were calculated using G–P fitting and the equations below [19].

$$\boldsymbol{B\,(E_{Ph}, X) = 1 + \frac{b-1}{K-1}\,(K^X - 1)\ for\ K \neq 1, B\,(E_{Ph}, X) = 1 + (b-1)x, K = 1}, \qquad \textbf{(15)}$$

$$\boldsymbol{k(E_{Ph}, X) = cX^a + d\,\frac{tanh\left(\frac{x}{XK} - 2\right) - tanh(-2)}{1 - tanh(-2)}\ for\ x \leq 40}, \qquad \textbf{(16)}$$

where E_{ph} is the photon's energy, x is the MFP's depth of penetration, and K (E_{ph}, X) is the dose-multiplier. EBF and EABF values plot with E_{ph} at 1, 5, 10, 15, 20, 25, 30, 35, and 40 MFP for all samples. The photoelectric effect, which is the dominant interaction in the low E_{ph} range, has caused a large number of photons to be absorbed, resulting in the lowest EBF and EABF values. This finding was previously accomplished using bismuth borate glasses [40]. EBF and EABF increase with increasing E_{ph} specially at middle energy and no significant change with doping ratio This is because Compton's predominance scatters the photon's energy [41]. Because pair production is the dominating interaction in the high-energy zone, the photons have been absorbed once more. Also, as shown in Figs. 13 (a-e), EBF depends deeply on MFP penetration depth having a range of (1.8- 81) at MFP range (1- 40). On the other hand, Fig. 14 (a-e) reveals that EABF values (1- 40) is (2.25-125) identified at a penetration depth of 40 MFP having value range .Because many scatterings occur at high penetration depths, the lowest values were detected at a 1 MFP penetration depth [40]. It has been observed that as the MFP is increased, the peak intensity increases. These surprising increments can be caused by the Ni-K-absorption element's edge as well as two peaks at 0.04 and 0.06 MeV [42].

3.3. Fast Neutron Removal Cross Section (FNRCS)

FNRCS stands for the possibility of neutrons passing through a substance without reacting. Calculating any absorber's R is as follows: [26, 42,43]:

$$\boldsymbol{\frac{\sum R}{\rho} = \sum_i w_i \left(\frac{\sum R}{\rho}\right)_i}, \qquad \textbf{(17)}$$

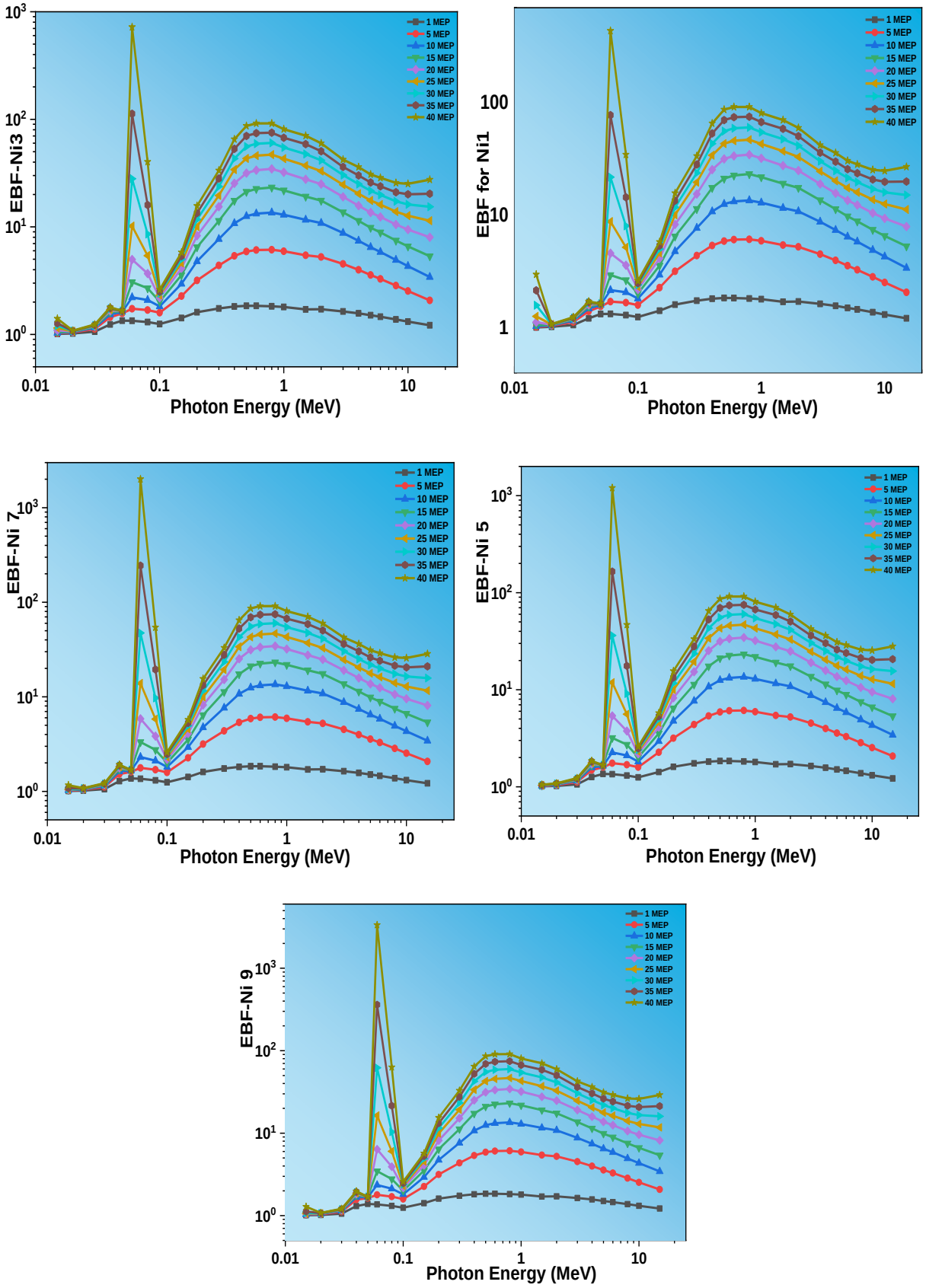

Fig. 13 (a-e): photon energy vs. EBF of samples at various MFP; a) Ni1; b) Ni3; c) Ni5; d) Ni7; and e) Ni9

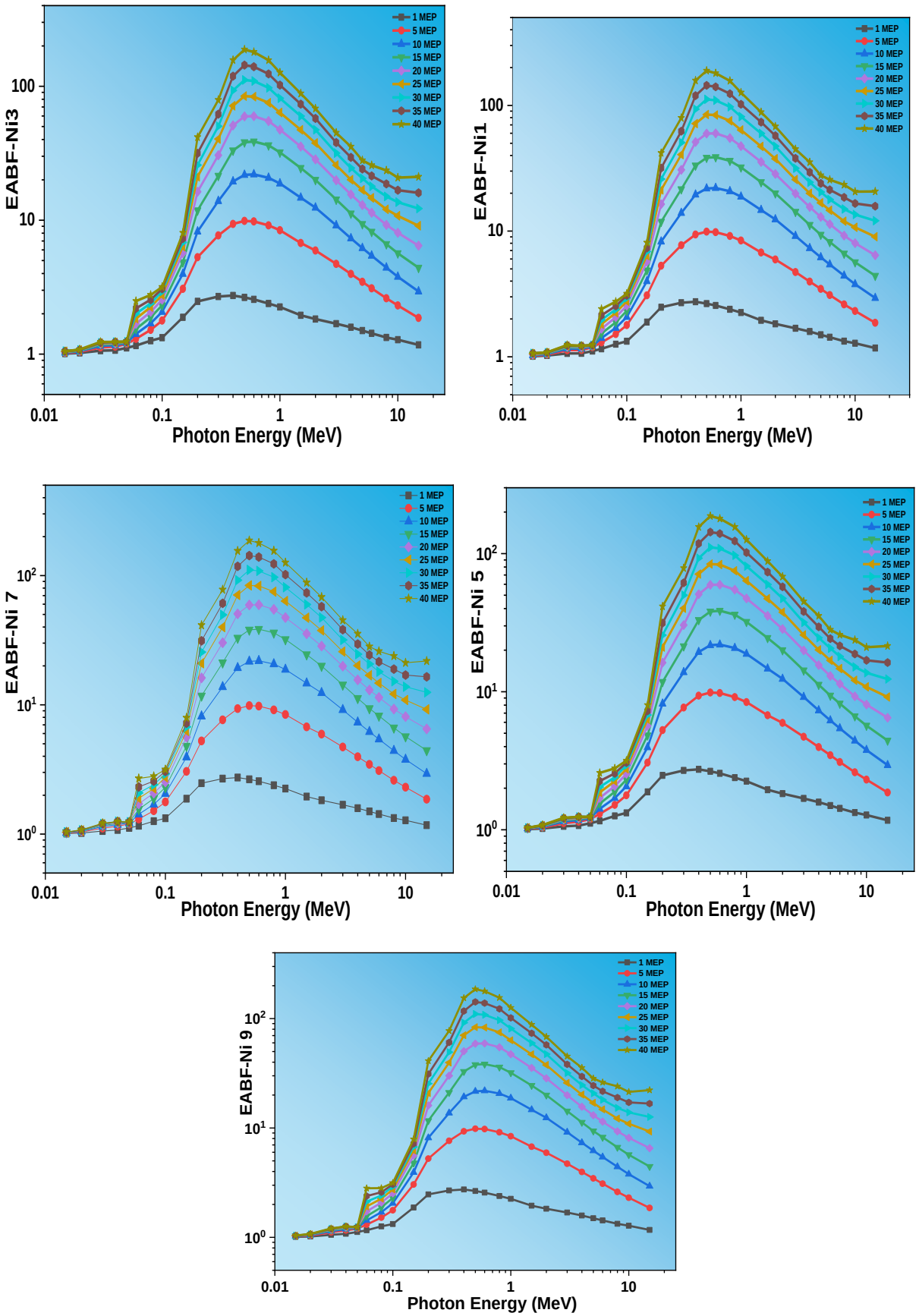

Fig. 14(a-e): photon energy vs. EABF of samples at various MFP; a) Ni1; b) Ni3; c) Ni5; d) Ni7; and e) Ni9

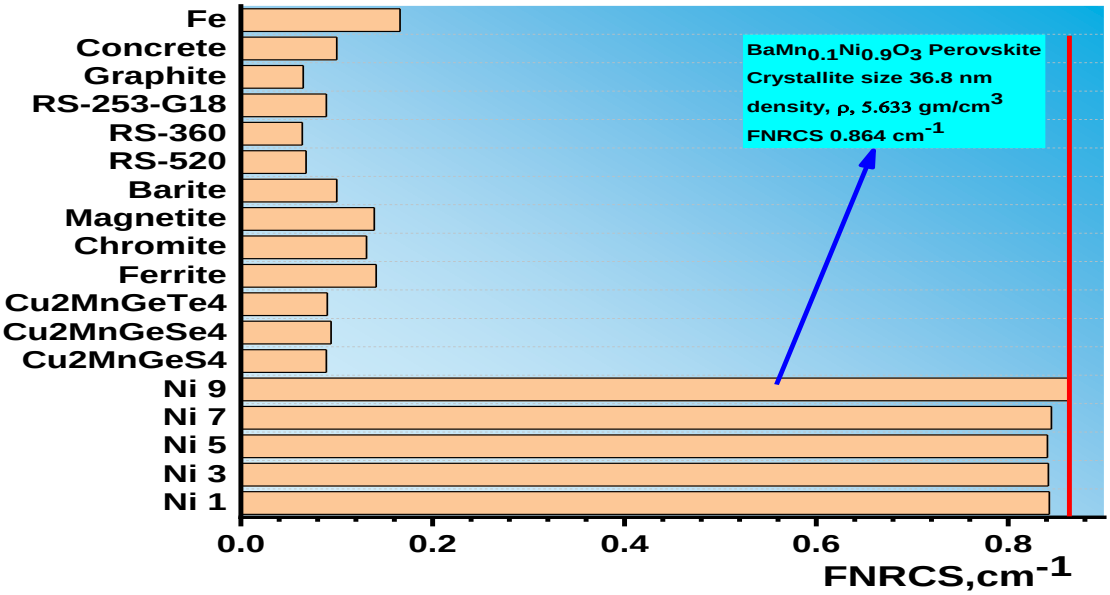

Fig. (15): FNRCS comparison for present samples and other materials

$$w_i = \sum_i w_i(\rho)_s; \qquad (18)$$

When $(\Sigma R/\rho)_i$ denotes the mass removal cross-section of the i^{th} component, (ρ_i) denotes the partial density, w_i denotes the weight fraction of the ith constituent (element or compound), and w_i denotes the partial density. The FNRCS values for the samples are 0.843, 0.842, 0.841, 0.845, and 0.864 cm^{-1} for Ni1, Ni3, Ni5, Ni7, and Ni9 respectively. FNRCS for the investigated materials was compared to marketable shielding glasses RS-253-G18, RS-360, and RS-520 [28], as well as Chromite, Ferrite, Magnetite, Barite, and Cu_2CoGeS_4, $Cu_2CoGeSe_4$, and $Cu_2CoGeTe_4$ semiconductor samples [26,28, 43]. Five examined samples exhibit FNRCS values that are higher than those of known shielding materials, as shown in Fig. 15. As shown in table2, our semiconductor compounds are superior to the competition in terms of neutron shielding.

4. CONCLUSION

Phy-X/PSD software is used to investigate the radiation attenuation properties of five semiconductor perovskite nano compounds at the E_{ph} range of 0.015–15 MeV. All parameters depend on photon energy. The studied energy range covers three main phenomena; photoelectric effect, Compton scattering and pair production. A minimum amount of photon absorption is seen when Eph is > 5 MeV because a considerable part of photons impinge on the material are scattered. HVL and MFP decreases by 6% with increasing Ni content from 10 to 90% which shows that these materials have effective radiation absorption qualities. Some parameters such as LAC, TVL, N_{eff}, ACS, ECS have no noteworthy change with Ni dopants. Z_{eff} increases by 45% with increasing Ni ratio from 10 - 90% . Buildup factors, EBF and EABF, possess the highest magnitude at a penetration depth of 40 MFPs, while the lowest values at a penetration depth of 1MFP. The samples' FNRCS values (0.80-0.86 cm^{-1}) are quite close to one another and show that perovskites have cross-section values that are larger than those of comparison materials by around 10 times, making them an excellent choice for applications requiring neutron shielding. Finally, our measurements revealed that $BaMn_{1-x}Ni_xO_3$ had good γ-ray and neutron detection over a wide energy range. This could be advantageous for nuclear medicine sensors, detectors, and applications.

REFERENCES

[1] Rajeshwari Mirji, Blaise Lobo" Study of polycarbonate–bismuth nitrate composite for shielding against gamma radiation" Journal of Radioanalytical and Nuclear Chemistry https://doi.org/10.1007/s10967-020-07038-3

[2] Hoda Alavian, Hossein Tavakoli-Anbaran" Study on gamma shielding polymer composites reinforced with different sizes and proportions of tungsten particles using MCNP code" Progress in nuclear energy 115 (2019) 91-98 – https://doi.org/10.1016/j.pnucene.2019.03.033

[3] M.A. Masoud, W.A. Kansouh, M.G. Shahien, K. Sakr, Alaa M. Rashad, A.M. Zayed" An experimental investigation on the effects of barite/hematite on the radiation shielding properties of serpentine concretes" Progress in Nuclear Energy 120 (2020) 103220- https://doi.org/10.1016/j.pnucene.2019.103220

[4] F. Akman, M.R. Kaçal, N. Almousa, M.I. Sayyed, H. Polat" Gamma-ray attenuation parameters for polymer composites reinforced with $BaTiO_3$ and $CaWO_4$ compounds" Progress in nuclear energy 121 (2020) 103257- https://doi.org/10.1016/j.pnucene.2020.103257

[5] N. Sabry, H.Y. Zahran, El Sayed Yousef, H. Algarni, Ahmad Umar, Hasan B. Albargi, I.S. Yahia" Gamma-ray attenuation, fast neutron removal cross-section and build up factor of $Cu_2MnGe[S,Se,Te]_4$ semiconductor compounds: Novel approach" Radiation Physics and Chemistry 179 (2021)109248 https://doi.org/10.1016/j.radphyschem.2020.109248

[6] B. Alim, E. Sakar, A. Baltakesmez, I. Han, M.I. Sayyed, L. Demir, Experimental investigation of radiation shielding performances of some important AISI-coded stainless steels: part I. Radiat. Phys. Chem. 166, 108455 (2020)

[7] Singh AK, Singh RK, Sharma B, Tyagi AK (2017) Characterization and biocompatibility studies of lead-free X-ray shielding polymer composite for healthcare application. Radiat Phys Chem 138:9–15

[8] Soylu HM, Lambrecht FY, Ersöz OA (2015) Gamma radiation shielding efficiency of a new lead-free composite material. J Radioanal Nucl Chem 305(2):529–534

[9] Fritz A. R. Schmidt "The attenuation properties of concrete for shielding of neutrons of energy less than 15 MeV" https://inis.iaea.org/collection/ NCLCollectionStore/Public/02/004/2004075.pdf

[10] El-Faramawy, N., Ramadan, W., El-Zakla, T., Sayed, M., El-Dessouky, M., Sakr, K., 2015. "Effect of ilmenite on the attenuation coefficient of gamma ray shielding cementitious matrix. Radiat. Eff. Defects Solids 170, 876–886.

[11] Sakr, K., Ramadan, W., Sayed, M., El-Zakla, T., El-Desouqy, M., El-Faramawy, N., 2018. Utilization of barite/cement composites for gamma ray's attenuation. Radiat. Eff. Defects Solids 173, 269–282.

[12] El-Khayatt, A.M., Ali, A.M., Singh, V.P., 2014. Photon attenuation coefficients of Heavy Metal Oxide glasses by MCNP code, XCOM program and experimental data: a comparison study. Nucl. Instrum. Methods Phys. Res. A 735, 207–212.

[13] MOHAMED METWALY Abu Anbar, 2015. The Pan-African Ophiolites and Related Mineralization in Egypt. Acta Geologica Sinica (English Edition), 89(supp. 2): 65-68.

[14] Baioumy, H.M., 2015. Rare earth elements, S and Sr isotopes and origin of barite from Bahariya Oasis, Egypt: implication for the origin of host iron ores. J. Afr. Earth Sci. 106, 99–107

[15] Rybkaa, A.V., Davydov, L.N., Shlyakhov, I.N., Kutny, V.E., Prokhoretz, I.M., Kutnya, D. V., Orobinsky, A.N., 2004. Gamma-radiation dosimetry with semiconductor CdTe and CdZnTe detectors. Nucl. Instrum. Methods Phys. Res. 531, 147–156

[16] I.I. Bashter, Calculation of radiation attenuation coefficients for shielding concrete. Ann. Nucl. Energy 24, 1389–1401 (1997)

[17] Ö. F. Özpolat, B. Alım, E. Şakar, M. Büyükyıldız, M. Kurudirek" Phy-X/ZeXTRa: a software for robust calculation of effective atomic numbers for photon, electron, proton, alpha particle, and carbon ion interactions" Radiation and Environmental Biophysics (2020) 59:321–329 https://doi.org/10.1007/s00411-019-00829-7

[18] Y. Harima, Y. Sakamoto, S. Tanaka, M. Kawai, Validity of the geometric-progression formula in approximating gamma-ray buildup factors. Nucl. Sci. Eng. 94, 24-35 (1986)

[19] E. Sakar, O.F. Ozpolat, B. Alim, M.I. Sayyed, M. Kurudirek, Phy-X/PSD: development of a user-friendly online software for calculation of parameters relevant to radiation shielding and dosimetry. Radiat. Phys. Chem. 166, 108496 (2020)

[20] M. H. Ghozza · I. S. Yahi . Synthesis, structure, electrical conductivity, and magnetic properties of $BaMn_{1-x}Ni_xO_3$ nano‑perovskite. Journal of the Australian Ceramic Society (2021) https://doi.org/10.1007/s41779-021-00670-6

[21] Quintero, M., Moreno, E., Alvarez, S., Marquina, J., Rincon, ´ C., Quintero, E., Grima, P., Heano, J., Macías, M.A., 2014. Lattice parameter

values and phase transitions for the Cu_2-Ii-Iv-S_4(Se_4) (Ii=Mn, Fe, Co; Iv=Si, Ge, Sn) magnetic semiconductor compounds. Rev. LatinAm. Metal. Mater. 34 (1). Caracas jun.

[22] Volodymyr Mosorov, The Lambert-Beer law in time domain form and its application, Appl. Radiat. Isot. 128 (2017) 1-5, https://doi.org/10.1016/ j. apradiso.2017.06.039.

[23] Y. Al-Hadeethi, M.I. Sayyed" X-ray attenuation features of some tellurite glasses evaluated at medical diagnostic energies" Applied Mathematics and Computation 365 (2020) 124712 - https://doi.org/10.1016/j.amc.2019.124712

[24] Y. Al-Hadeethi, M.I. Sayyed, O. Aga" Ionizing photons attenuation characterization of quaternary tellurite–zinc–niobium–gadolinium glasses using Phy-X/PSD software " Journal of Non-Crystalline Solids 538 (2020) 120044- https://doi.org/10.1016/j.jnoncrysol.2020.120044

[25] Cevik, U., Baltas¸, H., Çelik, A., Bacaksız, E., 2006. Determination of attenuation coefficients, thicknesses and effective atomic numbers for $CuInSe_2$ semiconductor. Nucl. Instrum. Methods Phys. Res. Sect. B Beam Interact. Mater. Atoms 247 (2), 173–179. https://doi.org/10.1016/J.NIMB.2006.01.064

[26] Sayyed, M.I., Kaky, Kawa M., S¸ akar, Erdem, Akbaba, Ugur, ˘ Taki, Malaa M., Agar, O., 2019. Gamma radiation shielding investigations for selected germanate glasses. J. Non-Cryst. Solids 512, 33–40. https://www.researchgate.net/publication/ 331733260.

[27] Elbashir, B.O., Sayyed, M.I., Dong, M.G., Elmahroug, Y., Lakshminarayana, G., Kityk, I. V., 2019. Characterization of Bi_2O_3–ZnO–B_2O_3 and TeO_2–ZnO–CdO–Li_2O–V_2O_5 glass systems for shielding gamma radiation using MCNP5 and GEANT4 codes. J. Phys. Chem. Solids. https://doi.org/10.1016/j.jpcs.2018.10.034

[28] Singh, H., Singh, K., Gerward, L., Singh, K., Singh Sahota, H., Nathuram, R., 2003. ZnO–PbO–B_2O_3 glasses as gamma-ray shielding materials. Nucl. Instrum. Methods Phys. Res. B. 207, 257–262. https://doi.org/10.1016/S0168-583X(03)00462-2.

[29] P. Kaur, D. Singh, T. Singh, Heavy metal oxide glasses as gamma rays shielding material, Nucl. Eng. Des. 307 (2016) 364–376.

[30] Al-Buriahi, M.S., Rammah, Y.S., Radiation sensing properties of tellurite glasses belonging to ZnO–TeO_2–PbO system using Geant4 code, *Radiation Physics and Chemistry* (2020), doi: https://doi.org/10.1016/j.radphyschem.2019.108632

[31] Prabhu, N.S., Hegde, V., Sayyed, M.I., Agar, O., Kamath, S.D., 2019. Investigations on structural and radiation shielding properties of Er^{3+} doped zinc bismuth borate glasses. Mater. Chem. Phys. 230, 267–276. https://doi.org/10.1016/j. matchem phys. 2019.03.074.

[32] Obaid, S.S., Sayyed, M.I., Gaikwad, D.K., Pawar, P.P., 2018. Attenuation coefficients and exposure buildup factor of some rocks for gamma ray shielding applications. Radiat. Phys. Chem. https://doi.org/10.1016/j.radphyschem.2018.02.026.

[33] Tekin, H.O., Kavaz, E., Altunsoy, E.E., Kilicoglu, O., Agar, O., Erguzel, T.T., Sayyed, M.I., 2019b. An extensive investigation on gamma-ray and neutron attenuation parameters of cobalt oxide and nickel oxide substituted bioactive glasses. Ceram. Int. 1–16. https://doi.org/10.1016/j.ceramint.2019.02.036

[34] Kavaz, E., Tekin, H.O., Agar, O., Altunsoy, E.E., Kilicoglu, O., Kamislioglu, M., Abuzaid, M.M., Sayyed, M.I., 2019. The mass stopping power/projected range and nuclear shielding behaviors of barium bismuth borate glasses and influence of cerium oxide. Ceram. Int. https://doi.org/10.1016/j.ceramint.2019.05.028.

[35] Cevik, U., Bacaksiz, E., Damla, N., Çelik, A., 2008. Effective atomic numbers and electron densities for CdSe and CdTe semiconductors. Radiat. Meas. 43, 1437–1442.

[36] Çelik, A., Çevik, U., Bacaksiz, E., Çelik, N., 2008. Effective atomic numbers and electron densities of $CuGaSe_2$ semiconductor in the energy range 6-511 keV. X Ray Spectrom. 37 (5), 490–494.

[37] H.C. Manjunatha, A study of gamma attenuation parameters in poly methyl methacrylate and Kapton, Radiat. Phys. Chem. 137 (2017) 254–259

[38] Devillers, M.A.C., 1984. Lifetime of electrons in metals at room-temperature. Solid State Commun. 49, 1019–1022

[39] M.S. Al- Buriahi, B. Tonguç, U. Perişanoğlu, E. Kavaz, The impact of Gd_2O_3 on nuclear safety proficiencies of TeO_2–ZnO–Nb_2O_5 glasses: A

GEANT4 Monte Carlo study, *Ceramics International* (2020),
doi: https://doi.org/10.1016/j.ceramint.2020.03.110.

[40] Manohara, S., Hanagodimath, S., Gerward, L., 2010. Radiat. Phys. Chem. 79 (5), 575.

[41] Lakshminarayana, G., Kumar, A., Lira, A., Dahshan, A., Hegazy, H.H., Kityk, I.V., Lee, D.-E., Yoon, J., Park, T., Comparative study of gamma-ray shielding features and some properties of different heavy metal oxide-based tellurite-rich glass systems, *Radiation Physics and Chemistry* (2020),
doi: https://doi.org/10.1016/j.radphyschem.2019.108633

[42] Tej Singh, Avijit Das, P.V. Varde, S. Battacharya" Neutron - Gamma Coupled Shielding Computer Code "SIGN" for Nuclear Reactor" Research Reactor Services Division, 2016, BARC, Mumbai-400085

[43] H.Y. Zahran, M.I. Mohammed, El Sayed Yousef, Mohammed S. Alqahtani, Manuela Reben, H. Algarni, Ahmad Umar, Hasan B. Albargi, I.S. Yahia, Mohamed Sh. Abdel-wahab, Medhat A. Ibrahim "Radiation attenuation properties of the quaternary semiconducting compounds Cu_2CoGe [S, Se, Te]$_4$" Results in Physics 37 (2022) 105488-doi.org/10.1016/j.rinp.2022.105488.